Dynamic MR Imaging using generalized series

*Neelam Sinha[*1], Manojkumar Saranathan[2] and A. G. Ramakrishnan[1]*

[1] Dept. of Electrical Engg., Indian Institute of Science, Bangalore 560012
[2] Lucas Center, Dept. of Radiology, Stanford University CA

Abstract. Dynamic MR Imaging can be achieved by sampling only selected regions in k-space. Optimal region selection in the 3D k-space needs to satisfy "maximum energy compaction" and "minimum acquisition" requirements. In this paper, a novel star-shaped truncation window is proposed to increase the achievable acceleration factor. The proposed window monotonically cuts down the acquisition of the number of k-space samples with lesser energy. The truncation window samples data within a star-shaped region centered around the origin in the k_y-k_z plane. The proposed window is experimentally found to capture more k-space energy compared to the other existing windows, for the same fraction of k- space acquisition. The missing values are extrapolated using generalized series modeling-based methods. The proposed method is applied to several real and synthetic data sets. The superior performance of the proposed method is illustrated using the standard measures of error images and uptake curve comparisons. Average values of slope error in estimating the enhancement curve are obtained over 5 real data sets of breast and abdomen images, for an acceleration factor of 8. The proposed method results in a slope error of 5%, while the values obtained using rectangular and elliptical windows are 12% and 10%, respectively.

Keywords: Dynamic MR, Sampling, Truncation Window

1. Introduction

Dynamic Magnetic Resonance Imaging is increasingly being used for functional studies where the organ being studied undergoes continuous change as in functioning of brain, cardiac activity and contrast agent uptake by suspected tumors. A very important application of dynamic imaging is Dynamic Contrast Enhanced MRI (DCE-MRI). It is used for detection and diagnosis of cancer. In DCE-MRI, a bolus of a paramagnetic contrast agent (typically, Gadolinium Chelate) is injected intravenously. The effect of the paramagnetic contrast agent is to shorten the relaxation times (T_1, T_2, and T_2*) of the hydrogen protons that are in the vicinity of the contrast agent. Generally T_1- weighted imaging sequences are preferred. Shorter T_1 values make tissues brighter, making the lesions appear brighter than the remaining tissues. The rate of contrast agent uptake by malignant lesions is significantly different from that of normal tissues because of their high vascularity. Malignant lesions can hence be detected by monitoring the rate of contrast agent uptake and their washout characteristics. This wash-in and wash-out phenomenon is monitored by a time series of images that continuously image the region of interest. Typical imaging protocols work as follows : Initially, a data set (pre-contrast data) is acquired with high spatial resolution. Subsequently, a contrast agent such as Gd-DTPA is injected followed by saline flush. The injections are immediately followed by acquisition of 4 or more post-contrast data sets, which takes a few minutes. The pre-contrast and the post-contrast image sets must be acquired with identical acquisition parameters. The signal intensity through the different types of tissues follow distinct characteristics as shown in Fig. 1.
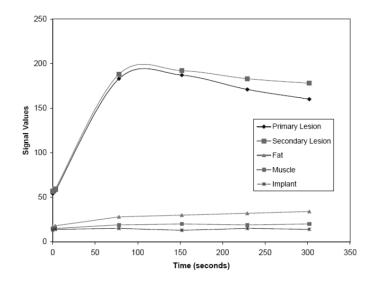
Fig. 1. Enhancement rates of contrast uptake for different types of tissues (Taken from [1])

2. Issues In DCE-MRI

The rate of uptake of contrast agent called "enhancement rate" is used to distinguish between malignant and benign tissues. The established way of measuring this is to calculate the slope of initial enhancement typically obtained by imaging the area of interest up to the time of peak enhancement (approximately 1.5 minutes), following the contrast injection. Beyond that time, signal intensity of normal tissues, which enhance slowly in the beginning will begin to approach that of malignant tissue. In order to differentiate between malignant and benign tissues by using the slope of initial enhancement, at least 4 time points must be sampled in 1.5 minutes implying a temporal resolution requirement of about 25 seconds. The exact temporal resolution required for the acquisition of the time series is determined by the time course of contrast agent uptake. Peak contrast enhancement in malignant lesions typically occurs about 90 seconds after injection, and hence to accurately determine lesions we need to acquire data sets well within that frame. As discussed earlier, the number of k-space points acquired determines the quality of the image obtained. Acquisition of fewer number of data points accelerates the process of data capture, but leads to Gibbs ringing and spatial blurring that significantly degrade the spatial resolution. On the other hand, acquiring many points in k-space leads to good image quality, but results in poor temporal resolution, that may not capture the uptake characteristics adequately enough. Thus we need to obtain good quality images with reduced data in order to satisfy the conflicting requirements of good spatial and temporal resolution. Reduction in the volume of data acquisition leads to faster scans. The objective of any dynamic imaging technique is to obtain as high an acceleration factor as possible, since it indicates the ability of the technique to yield high-quality images with reduced data (in turn, reduced acquisition time).

3. Techniques for DCE-MRI

Reduced data acquisition in conventional (sequential) MR scanners, where a single receiver coil is used, can be achieved either by acquiring only certain k-space regions or by regularly under-sampling the entire data in k-space. In this paper, our focus is on methods that follow the former approach. The two defining aspects in this approach are :

1) Optimal choice of k-space samples to be acquired
2) Technique to estimate the unacquired values

The criteria for optimal selection of samples in k-space are "maximum energy compaction" and "minimum acquisition". Partial data acquisition-based techniques hinge on the fact that if a small number of samples in k-space, containing a significant fraction of the total k- space energy, is captured at an adequate temporal resolution, then the dynamics of the sequence being imaged can be satisfactorily reconstructed. It is well-known that energy is concentrated at lower frequencies, and hence most acquisition schemes prioritize low frequency samples as against data at higher frequencies. The ratio of the total number of available k-space points to the number of points that are chosen to be acquired , is called the "acceleration factor". The techniques that result in higher acceleration factors are preferred. This is because, higher acceleration factors enable capturing the dynamic k-space at more number of time instants, thus resulting in higher temporal resolution.

The first of the reported dynamic imaging methods, proposed by van Vaals [2] was called "keyhole imaging". According to the scheme, only the pre-contrast data acquisition, which is free of time constraints, contains the entire range of k-space frequencies. During the course of contrast uptake, only partial k-space data, within a rectangular window symmetric about the k_x axis, is acquired. This rectangular window, at the center of the k_x-k_y-plane is assumed to contain a significant fraction of the signal energy. Image reconstruction using keyhole acquisition simply involves substitution of un-acquired dynamic k-space data with data from the fully acquired pre-contrast k-space data. Thus the dynamic images are obtained by direct substitution of the peripheral k-space of the pre-contrast acquisition. This technique suffers from the drawback posed by discontinuities in k-space incurred by direct substitution, which manifests as artifacts in the obtained images. The accuracy is limited by the size of the enhancing object and the rate of enhancement. An entirely different approach to dynamic imaging called "Continuous Update with Random Encoding" (CURE) was reported in [3]. In this approach, the k-space lines were randomly acquired with the low k-space being more frequently visited. The missing k-space points were substituted using their nearest k-space neighbours. Yet another approach for rapid acquisition called "Time-Resolved Imaging of Contrast Kinetics" (TRICKS) [4], followed segmenting the k-space, where not all the segments would be acquired at each time point. Instead, low k-space segments would be collected more frequently than the high k-space segments. The missing k-space data were estimated by interpolating between data that were collected. Variations of the keyhole method such as, keyhole with elliptical and rhomboid windows have also been proposed. The drawback with rhomboid window is that the maximum acceleration factor achievable is only 2. Experiments with elliptical windows have claimed better performance and higher acceleration factor due to the ability of the window to capture more k-space samples with higher signal energy. Another variation of this technique, called "Radial keyhole" was proposed [5]. Here, instead of a rectangular window, radial strips of data, whose centroid passes through the origin of k_y-k_z plane, are obtained. Here also, the missing high k-space values are obtained by replacement.

It must be noted that the methods discussed above differ in their choice of the optimal sampling region in k-space, but are similar in their choice of estimates of the un-acquired samples. A method to estimate the un-acquired samples more reliably than simple substitution was devised using generalized series modeling by Liang [6], called RIGR (Reduced-encoding Imaging by Generalized series Reconstruction). This method is based on the fact that, in applications as in DCE-MRI, the image morphology in the time-series does not drastically change from one image to another. Hence full k-space need not be acquired at every time point. A reference full k-space data set is first obtained at pre-contrast containing the stationary information. This acquisition is followed by partial (truncated by a rectangular window) data during the contrast uptake phase. In fact the data acquisition part is identical to that in keyhole imaging. RIGR differs in its approach to the estimation of the unacquired samples. The missing dynamic k-space

data is estimated with the basis functions of a generalized series model using the reference data and the partially acquired dynamic data. In the works reported in [7], [8] and [9], rectangular truncation window followed by RIGR-based extrapolation has been used. In [7] it is used to obtain dynamic images of liver. A full k-space post-contrast data set was used as the reference, and the temporal resolution reported is greater by a factor of 3. A variation of RIGR called "Two-reference RIGR" (TRIGR) was proposed for improved performance [10]. Here, two full k-space images are obtained, one in the pre-contrast phase, and the second at the end of the post-contrast phase. The dynamic images between the two full k-space images (references) are reconstructed using the difference image between the two references to construct the basis functions of the generalized series model.

These approaches result in reduced truncation artifacts compared to keyhole imaging. However, the drawback of these methods is that they tend to become unstable in the presence of noise, necessitating complicated regularization schemes for proper convergence. One of the recently proposed methods is called "Dynamic Imaging with Energy Matching" (DIEM) [11]. Here, data is acquired elliptically for each temporal phase during post-contrast. Two full k-space reference images are acquired: one at the beginning (precontrast) and the other during the post-contrast phase. The peripheral k-space dynamic data is estimated using a scaled version of the second reference data instead of direct replacement with the pre-contrast reference data. The energy of an outer annulus of the central k-space data (i.e. the acquired dynamic data) is compared to that of the post contrast reference and an energy scaling factor is computed as the square root of this ratio for each phase. Since the background signal causes significant errors in the computation of scaling factors, the pre-contrast reference is subtracted from the dynamic data for calculation of the energy scaling factors.

A very different approach was reported in [12], where a temporally enhancing lesion is considered as a two-dimensional space-time object possessing an associated spatio-temporal energy spectrum. The spatio-temporal space is segmented based on a threshold such that the total spectral energy in a finite number of k-space samples, constrained by the imaging experiment, is maximized. This thresholded map decides the k-space samples to be acquired at specific time instants. The acquisition scheme is shown to be adequate for a wide range of contrast-enhancing breast lesions.

In this paper, we propose a dynamic imaging scheme with a novel data truncation window. The proposed truncation window is aimed at increasing the achievable acceleration factor. The proposed window monotonically cuts down the acquisition of the number of k-space samples with lesser energy. The truncation window samples data within a star-shaped region centered around the origin in the k_y-k_z plane. The missing values are extrapolated using generalized series modeling-based methods.

4. Review of Generalized Series Modeling

Generalized series model is a general framework developed for constrained image reconstruction. The explanation that follows and the notations are adapted from [6] and [10]. The dynamic imaging problem is the acquisition of a sequence of q images, denoted as $I_1(x)$, $I_2(x)$…. $I_q(x)$, each of which is a snapshot of the time-varying image function I(x). Hence q data sets are acquired in k-space, $d_1(k)$, $d_2(k)$….$d_q(k)$ such that

$$d_q(k) = \int_{-\infty}^{\infty} I_q(x) e^{i2\pi kx} dx \qquad (1)$$

Here, the modeled image function I_{GS} is represented as

$$I_{GS}(x) = \sum_n c_n \phi_n(x) \qquad (2)$$

Here, $\Phi_n(x)$ are the basis functions given by $\Phi_n(x) = C(x)e^{2i\pi n\delta x}$, where the constraint function $C(x)$ is chosen to absorb the available apriori information and c_n are the weighting coefficients.

The generalized series framework is utilized for dynamic image reconstruction with as few phase encodings as possible. It relies on the fact that the evolving k-space cannot change much between two successive time instants. The two generalized series methods discussed below follow the framework discussed, but differ in their choice of constraint functions, and hence data acquisition schemes.

4.1 RIGR

In RIGR, data is acquired in the same way as in keyhole imaging. One full k-space (high-spatial resolution) data set is obtained before the injection of contrast, and several partial data sets are acquired during the course of contrast uptake and subsequent wash-out,. The full k-space data set serves as the initial estimate for the dynamically changing k-space that we set out to compute. Here, the constraint function $C(x)$ is chosen as an initial estimate of the desired function $I(x)$ and hence the optimal reconstruction is the one that maximizes the following cross-entropy measure,

$$-\int_{-\infty}^{\infty} I(x) \log \frac{I(x)}{C(x)} dx \qquad (3)$$

subject to the data consistency constraints

$$d(m\Delta k) = \int_{-\infty}^{\infty} I(x) e^{i2\pi m\Delta kx} dx \qquad (4)$$

The solution to the above constrained problem is

$$\hat{I}(x) = C(x) exp\left(\sum_n \lambda_n e^{i2\pi m\Delta kx}\right) \qquad (5)$$

where, λ_n are appropriate Lagrange multipliers.

If $C(x)$ is a good estimate for $I(x)$, then the power series expansion of the exponential term is approximated by the first two terms, resulting in

$$\hat{I}(x) \approx \sum_n [\delta(n) + \lambda_n] C(x) e^{i2\pi m\Delta kx} \qquad (6)$$

which turns out to be the same as the generalized series model functions $I_{GS}(x)$ in equation 2, with $c_n = \delta(n) + \lambda_n$

The unknown parameters c_n are determined by the system of linear equations as described later. Renaming the coefficients as

$$\hat{c}_0 = 1 + c_0 \qquad \text{and}$$

$$\hat{c}_n = c_n \qquad \text{for } n \neq 0$$

The GS model is rewritten as

$$I_{GS}(x) = C(x) + C(x) \sum_n \hat{c}_n e^{i4\pi n\Delta kx} \tag{7}$$

or in the data acquisition domain, we get

$$d_{GS}(k) = d_c(k) + \sum_n \hat{c}_n d_c(k - n\Delta k) \tag{8}$$

where $d_c(k)$ is the Fourier transform of $C(x)$.

The equation suggests that the high spatial-frequency data modeled by generalized series consists of two parts : The first part comes from the a priori information and the other part is adaptively adjusted through the coefficients to maintain data consistency. The spatial resolution of $I_{GS}(x)$ would be at least as good as that of $C(x)$. If a high spatial resolution reference image is acquired and used to define the basis functions, high spatial resolution dynamic images can subsequently be reconstructed from the generalized series model with only few dynamic encodings.

1) Determination of GS coefficients (c_n): The qth dynamic image I_q is such that, $d_q(k)$ is the Fourier transform $I_q(x)$. The generalized series coefficients are then given by,

$$d_q(m) = \sum_{n=-\frac{N_L}{2}}^{\frac{N_L}{2}-1} c_n d_c(m - n) \,, \qquad -\frac{N_L}{2} \leq m \leq \frac{N_L}{2} - 1 \tag{9}$$

where, N_L is the number of k-space lines acquired and $d_c(k)$ is the Fourier transform of $C(x)$.

4.2 TRIGR

A variation of RIGR called TRIGR, which stands for "Two-reference RIGR", was proposed in [10]. The data acquisition in TRIGR consists of two full k-space (high spatial resolution) data sets and several partial data sets (say, N_L lines are acquired in k-space). Here, reconstruction of dynamic images is accomplished using the generalized series model with a reference image reflecting the areas of change in the sequence of images. The difference reference image is constructed using the baseline and active reference images using the full set of encodings and subtracting the complex images. The dynamic difference data ($d_{diff}(k)$) is created as,

$$d_{diff}(k) = d_{dyn}(k) - d_{baseline}(k) \tag{10}$$

where, $d_{dyn}(k)$ is the dynamic data and $d_{baseline}(k)$ represents the corresponding part of the baseline reference encoding. The RIGR model then becomes

$$I_{diff}(x) = |I_{ref}(x)| \sum_{n=-\frac{N_L}{2}}^{\frac{N_L}{2}-1} c_n e^{i2\pi n\Delta kx} \tag{11}$$

where, $I_{ref}(x)$ is the difference reference image and N is the number of dynamic encodings.

The coefficients c_n are obtained by fitting the difference data to maintain consistency of the data.

$$a_{diff}(m) = \sum_{n=-\frac{N_k}{2}}^{\frac{N_k}{2}-1} c_n d_{ref}(m-n)$$

(12)

where, $d_{ref}(m-n)$ is the difference data created by subtracting the baseline and active reference data sets. The dynamic image is generated by adding the complex dynamic difference image to the baseline reference image. Hence the dynamic image $I_{dyn}(x)$ is given as

$$I_{dyn}(x) = I_{diff}(k) + I_{baseline}(x)$$

(13)

5. The Case for a New Data Truncation Window

Data truncation windows are used for partial data acquisition in order to acquire samples within a chosen region in the k-space. Partial data acquisition is always carried out such that fewer values are captured along either k_y or k_z. The fact that more signal energy is concentrated at lower frequencies (low k-space), compared to higher frequencies (high k-space), has led to acquisition schemes designed to capture more points in low k-space.

5.1. Rectangular (RS) and Elliptical (ELL) windows

The most commonly used data truncation window is "rectangular" in shape (RS), as shown in Fig. 2 (a). A variation of the rectangular window, called the "elliptical" (ELL) window is also in use (shown in Fig. 2(b)), which prioritizes points based on the radial distance from the origin in the k_y-k_z plane. For higher fractions of k-space availability, the two masks look similar, as the curvature of the ellipse straightens. Another variation of the RS truncation window is the "rhomboidal" window, where the four vertices of the rhombus touch the four edges of the k_y-k_z plane. Each of the windows has a trade-off between the maximum acceleration factor possible and the fractional energy captured. Here, we explore the usage of a novel window, called the "star-shaped" window.
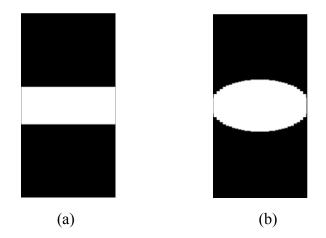

(a)   (b)

Fig. 2   Examples of widely utilized data truncation windows in k_y-k_z plane
(a) rectangular (RS) (b) elliptical (ELL)

5.2 Star-shaped data truncation window

The star-shaped (SS) data truncation window, (see Fig. 3) consists of 4 arms all along the k_y-k_z axes. The window is so shaped that it captures greater number of points near the origin, while the number of data points tapers off as we move away from the origin. We observe that the SS data truncation window retains those points in the k_y-k_z plane, whose one or both co-ordinates lie in the low-frequency range. Besides, as we increase the fraction of k-space available, the data truncation window expands near the origin, leading to acquisition of many more points in the desired low k-space. Hence, we expect this mask to be able to capture a greater fraction of the k-space energy, for a given fraction of k-space availability. In acquisitions where the data is not too noisy, it is expected that the acquisition-scheme that optimizes the "highest-energy capture" criterion results in the best image reconstruction, for a given fraction of the k-space availability. A comparison of percentage of energy captured by the 3 masks, namely, SS, ELL and RS as a function of the percentage of k-space points acquired, is presented on a synthetic and several real data sets. We leave out the rhomboidal mask, since it can only give an acceleration factor of 2. As can be seen from Figs. 4, 6, 5 and 7, the SS-mask consistently captures more k-space energy at lower fractions of k-space availability, leading to the conjecture that it might lead to better image reconstruction. It may also be observed that the ELL mask captures more k-space energy than the RS mask for lower fractions of k-space availability. However, as the fraction of k-space availability increases, the energy captured by RS and ELL masks become comparable.
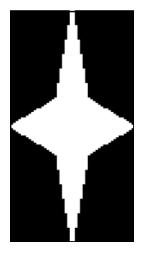

Fig.3   Proposed data truncation window in k_y-k_z plane : star-shaped (SS) mask

6. Data Analysis

All simulations are carried out in MATLAB. The proposed method is applied to a synthetic phantom as well as real data volumes of breast and abdomen. In our experiments, we have used both the extrapolation techniques, RIGR and TRIGR. The implementation of the extrapolation techniques utilized the fast versions of the algorithms as given in [13]. The partial data sets obtained by using the proposed star-shaped window as well as the rectangular and elliptical windows were utilized. The criteria used to assess the performance of the methods include :

- Faithful reproduction of enhancement curves (Error in slope calculation)
- Difference images with respect to the original ("gold-standard") image
- Profile comparison of scan lines

The analysis of different data sets is presented on a case-by-case basis.

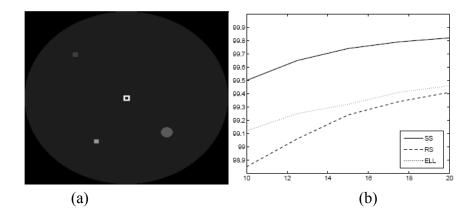(a)   (b)

Fig. 4. Comparison of energy captured by various masks on a phantom data set. (a) Mid-slice of the phantom. (b) Corresponding plot of percentage of energy (along Y -axis) vs. percentage of k-space acquired (along X-axis).

(a)   (b)

Fig. 5. Comparison of energy captured by various masks on a real data set (breast). (a) Original image of the real data set (breast with a large tumor shown by the arrow). (b) Corresponding plot of percentage of energy (along Y -axis) vs. percentage of k-space acquired (along X-axis).
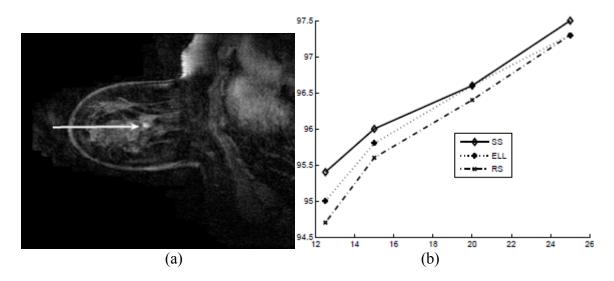
Fig. 6. Comparison of energy captured by various masks on another real data set (breast). (a) Original image of the real data set (Breast with a small tumor shown by the arrow). (b) Corresponding plot of percentage of energy (along Y -axis) vs. percentage of k-space acquired (along X-axis).
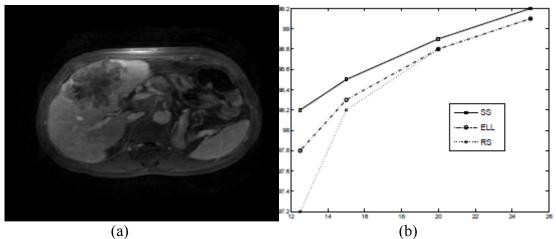

Fig. 7. Comparison of energy captured by various masks on a typical abdomen data set. Original image. (b) Corresponding plot of percentage of energy (along Y -axis) vs. percentage of k-space acquired (along X-axis).

6.1. Synthetic data

The proposed method was first applied on a noisy synthetic data set, for proof of concept. The phantom is constructed with tumors of various sizes and shapes, enhancing at different rates (see Fig. 4(a)). The data set is of dimensions 256 x 256 x 20, along X, Y and Z axes respectively. The evolving k-space is captured at 7 time instants. To simulate reduced data sets, the respective masks are applied to the full data set, resulting in the desired partial data set. Reconstruction using RIGR and TRIGR were carried out using various fractions of k-space availability. The objective is to look into acceleration factors of at least 4, translating to assuming k-space acquisitions of 25% and below. The most-challenging part of the phantom reconstruction is the rim-enhancing (annular) tumor, right at the center of the slice seen in Fig. 4(a).

Case (i) : RIGR reconstruction

The results are shown for 20% of k-space availability. A close look at the error images in Fig. 8 clearly shows the differences in the images reconstructed. It should be noted that the maximum error in the difference images occur at the annular tumor. The error image using the SS mask shows the least amount of ripples, while the other masks show substantial ringing at abrupt transitions. The profile reconstruction in Fig. 9, through a tumor clearly shows ripples in the RS reconstruction, while the SS and ELL masks follow the abrupt change in intensity more faithfully.

Case (ii) : TRIGR reconstruction

The results are shown for 20% of k-space availability. A close look at the error images in Fig. 10 clearly shows the better quality of reconstructed images as compared to the corresponding images obtained using RIGR. The SS mask results in better image reconstruction as compared to ELL and RS masks. The profile reconstruction in Fig. 11 through a tumor clearly shows ripples in the RS reconstruction, while the SS and ELL masks follow the abrupt change in intensity more faithfully. In this case, unlike RIGR, it must be noted that while the SS mask performs the best, the performances of RS and ELL masks are comparable.

6.2. Real data

Five real data volumes comprising 2 breast data sets and 3 abdomen data sets are analyzed. Among the breast data sets, one of them contains a large enhancing tumor while the other contains a small tumor. The abdomen data sets are all similar with no enhancing tumors, but contain enhancing blood vessels.
1) Breast data with large tumor: This data set is of dimensions 256 x 256 x 36. The 21st slice has a large tumor occupying about 300 pixels out of 256 x 256, which is shown in Fig. 5(a). The image shown has perceptibly high SNR. We expect the reconstruction of these images to be good, not only because of the signal quality, but also because of the large size of the tumor. The dynamic volume is available at 5 time points.

Case (i) RIGR reconstruction : The first volume is chosen as the high spatial-resolution data set, and the remaining 4 volumes are reduced according to the 3 masks considered. The reconstructed images obtained with 20% of k-space availability are shown in Fig. 12. As is noticed, all the 3 masks perform comparably well and result in satisfactory quality of reconstructed images. However, the reconstruction using RS mask looks blurred as compared to the reconstruction with other masks. The plot shown in Fig. 13(a) is obtained from the images (shown in Fig. 12) reconstructed with 20% of the k-space,. The plot suggests that all the phases are satisfactorily reconstructed. The plot in Fig. 13(b) clearly shows that the enhancement curve slope error is well within 10%, even for cases where only 10% of k-space is available. Hence, acceleration factors of even 10 can be achieved on data sets of this nature.

Case (ii) TRIGR reconstruction : The first and the last volume are chosen as the high spatial resolution data sets, and the remaining 3 are reduced according to the 3 masks considered. The performance of both RIGR and TRIGR are comparable in such a noise-free, large tumor data. Differences in performances can be expected at very high acceleration factors. However, we do not consider cases of very high acceleration factor (8 and above) because, the SNR of the data acquisition would be very low.

2) Breast data with small tumor : This data set is of dimensions 256 x 256 x 20. The 11th slice has a tumor as shown in Fig. 6(a). The images are noisy, and the tumor is very small, occupying about 15 pixels out of 256 x 256. The dynamic volume is available at 4 time points.
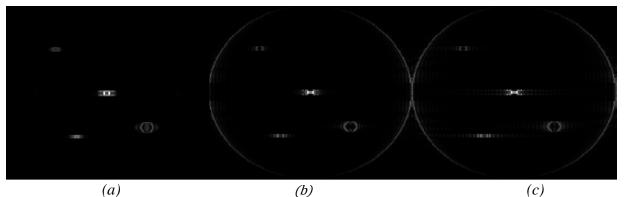
(a) *(b)* *(c)*

Fig. 8. Comparison of performance of different masks on the synthetic data set shown in Fig. 2.4(a) for an acceleration factor of 5. Error images for RIGR reconstruction using masks (a) SS (b) ELL (c) RS (color scale for all images : 0 to 16)
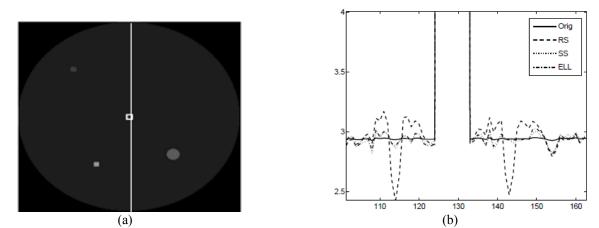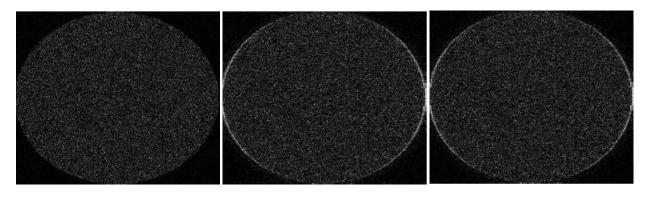

(a) (b)

Fig. 9. Comparison of a scan line through the annular tumor for the RIGR reconstructions obtained using different mask. (a) Original image with the scan line marked in white (b) Reconstruction of the scan line using different masks

(a) *(b)* *(c)*

Fig. 10. Comparison of performance of different masks on the synthetic data set shown in Fig. 4(a) for acceleration factor 5. Error images for TRIGR reconstruction using masks (a) SS (b) ELL (c) RS (color scale for all images : 0 to 14)
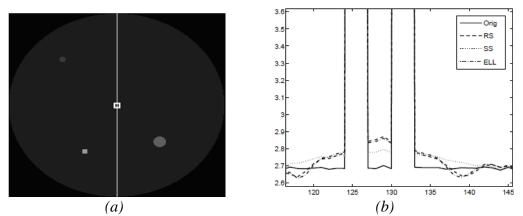
(a)   *(b)*

Fig. 11. Comparison of a scan line through the annular tumor for the TRIGR reconstructions obtained using different masks. (a) Original image with the scan line marked in white (b) Reconstruction of the scan line using different masks

(a)   *(b)*   *(c)*
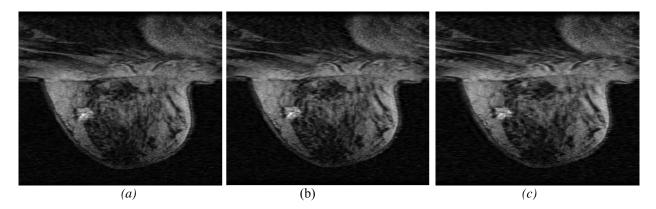
Fig. 12. Performance on the real breast data set with large tumor (shown in Fig. 5(a)): Comparison of images reconstructed using RIGR with various masks : (a) SS (b) ELL (c) RS. (color scale for all images : 0 to 255)
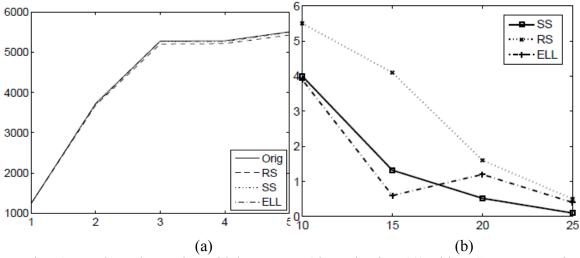

(a)   *(b)*

Fig. 13. Results on breast data with large tumor (shown in Fig. 5(a)) with RIGR reconstruction. (a) Comparison of the enhancement curves through the tumor (b) Comparison of the percentage uptake slope error (along Y-axis) vs. percentage of k-space sampled (along X-axis)

Case (i) RIGR reconstruction : The first volume is chosen as the high spatial-resolution data set, and the remaining 3 are reduced according to the 3 masks considered. Since the images are noisy, the regularization parameter in RIGR has to be fine-tuned. The errors in the reconstructed images seen in Fig. 14 are obtained with 20% of k-space availability. Here it is seen that SS and RS masks perform much better than the ELL mask. The plot in Fig. 15 clearly shows that the enhancement curve slope error is within 10% of error, only for k-space available of 15% and above. Hence, acceleration factors greater than 6 would lead to erroneous reconstructions. It is also observed that using SS mask results in least values of slope errors. As observed in the error images in Fig. 14, it is noticed that the ELL masks results in the highest error compared to the other masks.
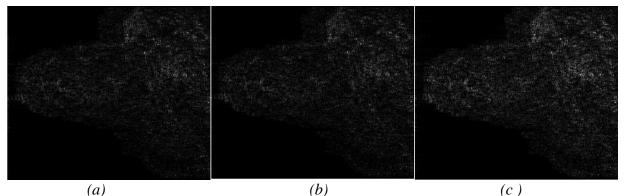
Case (ii) : TRIGR reconstruction : The first and the last volume are chosen as the high resolution data sets, and the remaining 2 are reduced according to the 3 masks considered. The plot of the error in enhancement slope versus fraction of k-space acquired shows that the performance using TRIGR is found to be better than that obtained using RIGR. The plot shown in Fig. 16(a) is obtained after reconstruction using 25% of the k-space. The plot suggests that the third phase is not as well reconstructed as the second. The plot in Fig. 16(b) clearly shows that the enhancement curve slope error is within 10% of error, even for fractions as small as 12.5% indicating a higher achievable acceleration factor, as compared to the technique using RIGR. Consistent with RIGR reconstructions, it is seen that the SS and RS masks perform better than the ELL mask.
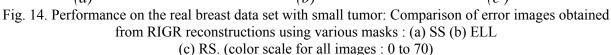
3) Abdomen data: Three abdomen data sets of which 2 of them are of dimensions 256 x 256 x 20, while the other is of dimensions 256 x 256 x 36. All the 3 data sets are analyzed using the proposed technique. ROIs of different sizes are chosen in order to assess the accuracy and resolution of the reconstruction techniques. Enhancing structures (like blood vessels) are used as ROIs. Signal enhancement curves through the ROIs are used to compute errors in the slope of contrast uptake. The difference images are also examined for reconstruction quality and artifacts. Large ROIs typically occupy 100 pixels and above, while small ROIs occupied about 20 pixels. In order to calculate mean slope errors, ROIs from all the 3 data sets are analyzed, and the mean of the statistics is calculated. A typical image in the data sets utilized is shown in Fig.7(a). The corresponding plot of the k-space energy captured by the various masks for different fractions of k-space acquisition is shown in Fig.7(b).

Case (i) : RIGR reconstruction : At k-space availability of 20% and above, all the masks perform comparably well, with the slope errors well-within bounds of 10%. However, differences can be observed in the values of slope errors for varying sizes of ROI.

Case (ii) TRIGR reconstruction : At k-space availability of 20% and above, all the masks perform comparably well, with the slope errors well-within bounds of 10%. However, differences can be observed in the calculation of slope errors for different sizes of ROI. Fig. 17 compares the error images obtained from the images reconstructed using TRIGR with different masks, for a real abdomen data set.

Clearly, plots in Figs. 18 and 19 show that the performance using TRIGR outperforms that of RIGR. For a given acceleration factor, reconstruction using TRIGR results in far less errors than RIGR. The plot in Fig. 19(a) shows that if the ROI in question is known to be large before hand, then even acceleration factors of 8 are achievable, since the slope errors are negligible. But if the ROI happens to be small (see plot in Fig. 19(b)), then SS mask performs better. Average values of slope error in estimating the enhancement curve are obtained over 5 real data sets of breast and abdomen images, for an acceleration factor of 8. The proposed method results in slope error of 5%, while the values obtained using rectangular and elliptical windows are 12% and 10%, respectively.
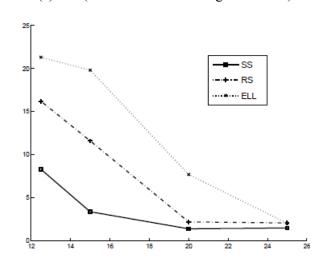
(a)	*(b)*	*(c)*

Fig. 14. Performance on the real breast data set with small tumor: Comparison of error images obtained from RIGR reconstructions using various masks : (a) SS (b) ELL (c) RS. (color scale for all images : 0 to 70)

Fig. 15. Comparison of the percentage uptake slope error vs. percentage of k-space available with RIGR reconstruction, for breast data with small tumor.
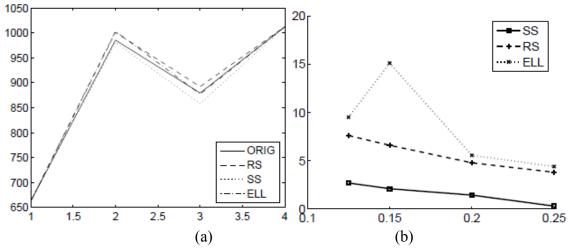

(a)	*(b)*

Fig. 16. (a) Comparison of the enhancement curves (signal intensity vs. sampling instants) through the tumor in the TRIGR reconstructed images of the data shown in Fig. 6(a). (b) Corresponding plot showing comparison of the percentage uptake slope error vs. fraction of k-space available.
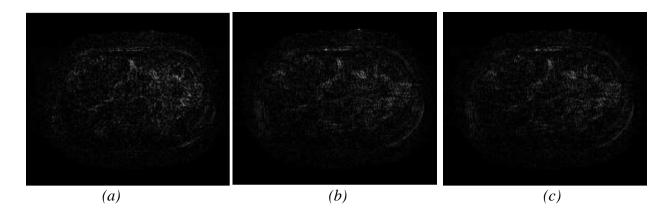
(a)   *(b)*   *(c)*

Fig. 17. Performance on a real abdomen data set : Comparison of error images using TRIGR with various masks : (a) SS (b) ELL (c) RS (color scale for all images : 0 to 50)
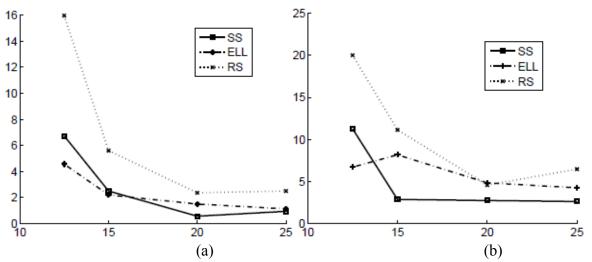

(a)   (b)

Fig. 18. Mean percentage slope errors vs. percentage of k-space sampled on real data sets of abdomen using RIGR (a) Large ROI (100 pixels) (b) Small ROI (20 pixels)
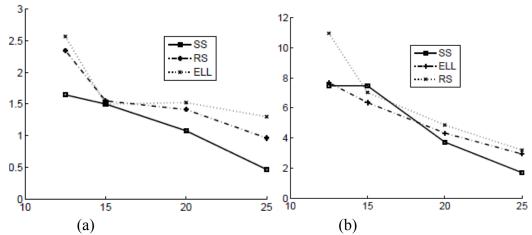

(a)   (b)

Fig. 19. Mean percentage slope errors vs. percentage of k-space sampled on real data sets of abdomen using TRIGR reconstruction (a) Large ROI (100 pixels) (b) Small ROI (20 pixels)

7. Discussion

As seen from the experiments, reconstructions using TRIGR outperform the corresponding images obtained using RIGR. This is to be expected since TRIGR involves acquisition of 2 full k-space data sets. The error images obtained from the reconstructions and the errors in slope of contrast uptake are found consistently to be much better with TRIGR reconstructions. It can be observed that higher acceleration factors are possible when TRIGR is utilized along with the proposed SS data truncation window. It is also seen that the quality of image reconstruction obtained depends on the fraction of k-space acquired and the relative size of the region of interest in the image. The SNR of the acquired data also plays a critical role in the quality of the reconstructed image. For cases where the SNR is very low, larger fractions of k-space need to be acquired to obtain images of diagnostic quality. On the other hand, for higher values of SNR, lower fractions of k-space acquisition may suffice. In the former case, increase in the fraction of acquired k-space leads to visible improvement in image quality obtained, while in the latter, increase in the fraction of acquired k-space may not lead to perceptible improvement in the quality of the reconstructed image. In the comparison of scan lines through regions of abrupt transitions, the image reconstruction using RS mask shows far greater ripples than the other two masks. In some cases it is observed that, contrary to expectation, when the fraction of acquired k-space increases, the reconstruction error also increases. This could be attributed to the possibility of increase in noise, in place of signal, in the acquisition.

8. Conclusion

In this paper, a novel star-shaped truncation window is proposed to increase the achievable acceleration factor. The proposed window monotonically cuts down the number of samples acquired in k-space regions with lesser energy. The truncation window samples data within a star-shaped region centered around the origin in the k_y-k_z plane. The missing values are extrapolated using generalized series modeling-based methods. The proposed method is applied to several real and synthetic data sets. The superior performance of the proposed method is illustrated using the standard measures of error images and uptake curve comparisons. Average values of enhancement curve slope error over 5 real data sets of breast and abdomen images are compared for an acceleration factor 8.. The proposed method results in an error of 5%, while those obtained using rectangular and elliptical windows are 12% and 10%, respectively.

9. References

[1]   R. Edward Hendrick, "Breast MRI: Using physics to maximize its sensitivity and specificity to breast cancer," Tech. Rep., Northwestern University Feinberg School of Medicine, 2004, 46*th The American Association of Physicists in Medicine (AAPM) Annual Meeting*.

[2]   J. J. van Vaals, "Keyhole method for accelerating imaging of contrast uptake," *Journal of Magnetic Resonance Imaging*, vol. 3, pp. 671–675, 1993.

[3]   T. Parrish and X. Hu, "Continuous update with random encoding (CURE): A new strategy for dynamic imaging," *Magnetic Resonance in Medicine*, vol. 33, pp. 326–336, 1995.

[4]   F. R. Korosec, R. Frayne, T. M. Grist, and C. A. Mistretta, "Time-resolved contrast-enhanced 3d MR angiography," *Magnetic Resonance in Medicine*, vol. 36, pp. 345–351, 1996.

[5]   N. Mistry, J. Pollaro, J. Song, and G. A. Johnson, "Interleaved radial imaging with sliding window-keyhole reconstruction to image pulmonary perfusion in rats," ISMRM Workshop on Non-Cartesian Imaging, 2007.

[6]   Z. P. Liang and P. C. Lauterbur, "An efficient method for dynamic magnetic resonance imaging," *IEEE*

Transactions on Medical Imaging, vol. 13, no. 4, pp. 677–686, 1994.

[7]   M. J. White, M. Bourgeois, D. M. Koh, A. Degenhard, L. Moore, D. Collins, and M. O. Leach, "Rapid dynamic contrast enhanced MRI using reduced acquisition and constrained reconstruction: pilot work for dynamic liver study," Pro*ceedings of Medical Image Understanding and Analysis* (MIUA), pp. 37–40, 2002.

[8]   Y. Sun, D. Yang, Q. Ye, M. Williams, J. M.F. Moura, F. Boada, Z. P. Liang, and C. Ho, "Improving spatiotemporal resolution of USPIO-enhanced dynamic imaging of rat kidneys," *Magnetic Resonance Imaging*, vol. 21, pp. 593–598, 1994.

[9]   Z. P. Liang, "Generalized series dynamic imaging," *Proceedings of International Workshop on Medical Imaging and Augmented Reality,* pp. 145–151, 2001.

[10]   Z. P Liang J. M. Hanson, E. C. Wiener, and P. C. Lauterbur, "Fast dynamic imaging using two reference images," *Magnetic Resonance in Medicine,* vol. 36, pp. 172–175, 1996.

[11]   S. K. Shripad, "Dynamic contrast-enhanced magnetic resonance imaging," M.S. thesis, Department of Electrical Engineering, Indian Institute of Science, Bangalore, India, 2004.

[12]   T. L. Chenevert S. Krishnan, "Spatio-temporal bandwidth-based acquisition for dynamic contrast-enhanced magnetic resonance imaging," *Journal of Magnetic Resonance Imaging*, vol. 20, no. 1, pp. 129–137, *2004.*

[13]   Z. P. Liang, Bruno Madore, Gary H. Glover, and Norbert J. Pelc, "Fast algorithms for GS-model-based image reconstruction in data-sharing Fourier imaging*," IEEE Transactions on Medical Imaging,* vol. 22, no. 8, pp. 1026–1030, 2003.